SUPPLEMENTARY INFORMATION

doi:10.1038/nature11072

"Thermal and Electrical Transport across a Kondo-breakdown Quantum Critical Point"

I. BACKGROUND

The low-temperature behaviour of the heavy-fermion metal $YbRh_2Si_2$ was studied by means of thermal and electrical transport across its field-induced quantum critical point (QCP). The thermal conductivity of metals is typically measured down to temperatures in the Kelvin range.[1,2] Because of the low energy scales, measurements in the heavy-fermion metals have been extended down to temperatures as low as 0.06 K (Ref. 3) or even 0.04 K (Ref. 4). In our case, special efforts have been made to measure the thermal conductivity at $B = 0$ and 0.02 T down to 0.025 K due to the very low Néel temperature $T_N = 0.07$ K (at $B = 0$). Furthermore, we have performed substantially more temperature scans for $B = 0$ in order to reduce the statistical error of the data. At $B = 0.06$ T, which is close to the critical field B_c, we were able to measure the thermal conductivity down to 0.04 K. At higher fields, the measurements of the thermal conductivity were performed down to 0.06 K.

II. CONTACTS

Previous thermal transport studies pointed out the strong influence of thermal contact resistances and demonstrated the necessity of a careful contact preparation.[3,5] Subsequent to polishing the $YbRh_2Si_2$ sample (sample 1) for optimization of their geometry for our measurements, the sample surface was cleaned in an ultrasonic bath and rinsed in ethanol. The contact pads were prepared by evaporating a gold film (thickness of $\approx$ 50 nm) and applying a lift-off technique which allowed for optimum pad width and separation. Gold evaporation was conducted by using electron beam evaporators in ultra-high vacuum which turned out to provide superior contacts compared to thermal evaporation. Gold wires (50 μm) were then attached to the contact pads by silver paint to make use of the pad area. The silver paint covered an area of width of about 130 μm, which is very small compared to the distance between the contacts (2.9 mm). This contributes to a systematic standard error of about 4.5% in the estimation of the geometry factor. It is the same for all experiments. We did not observe any indication of diminished thermal conductivity due to contact resistances down to 0.025 K. The same contacts were used for thermal and electrical conductivity measurements.

III. SYSTEMATIC ERRORS

Although most measurements were performed on a sample cut specifically for thermal transport, sample 1 ($4.2\times0.5\times0.1$ mm^3), additional electrical resistivity measurements were done on a second sample (sample 2) with average size $1.7 \times 0.41 \times 0.06$ mm^3 from the same piece of crystal. This was necessary to systematically study the dependency of the low-T electrical resistivity on the current, *cf.* Section IV. Because of the inhomogeneous thickness of the samples, the geometry factor could not be determined with very high precision. However, the measured resistivities could perfectly be rescaled by a

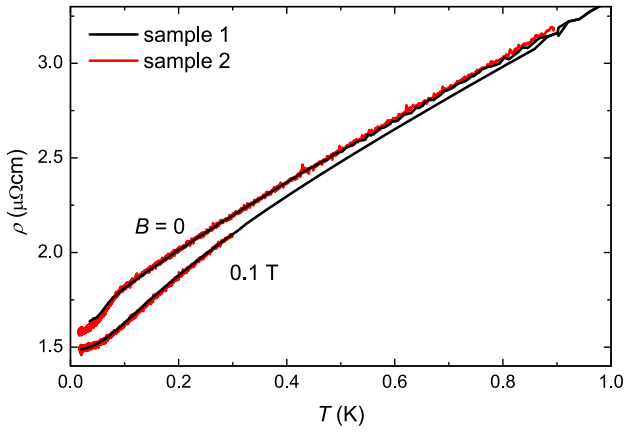

FIG. S1: Temperature dependency of the electrical resistivities of two $YbRh_2Si_2$ single crystals from the same batch. The data of sample 2 have been multiplied by a factor 1.25 ± 0.03 and corrected by a difference in residual resistivity of 0.22 $\mu\Omega$cm.

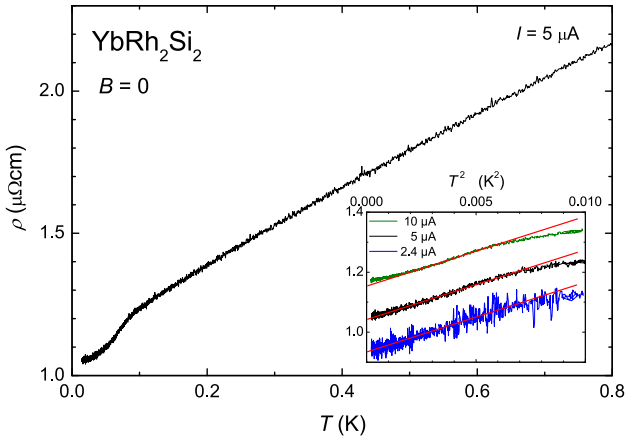

FIG. S2: Temperature dependency of the electrical resistivity of sample 2. The kink at about 0.07 K indicates the Néel temperature T_N . Below T_N a T^2 dependency of the resistivity is observed as expected[6] (*cf.* inset where the individual curves are shifted vertically).

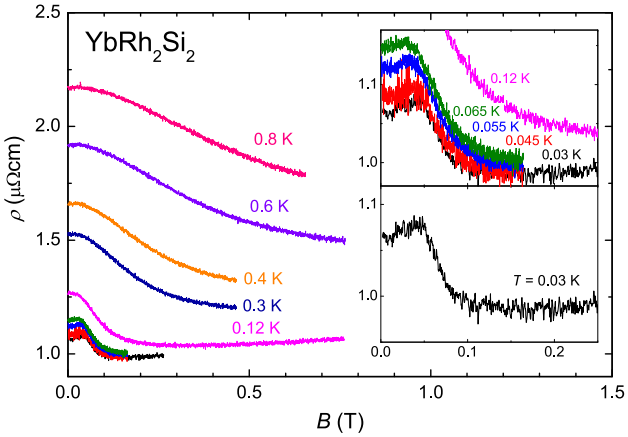

FIG. S 3: Magnetoresistivity of sample 2 measured with a current of 5 μA. The upper inset magnifies the low field, low temperature region of the main panel to emphasize that the magnetoresistivity is positive inside the AF phase, but exhibits a rapid drop across a crossover field B^*. This is further illustrated in the lower inset for our lowest temperature $T = 0.03$ K. The rapid crossover across B^* was systematically analysed[9,10]; in the zero-temperature limit, it corresponds to a sharp jump because the crossover width extrapolates to zero. The low-temperature data are also consistent with the existence of a peak in the residual resistivity as a secondary feature superimposed on the sharp jump, although its interpretation is not clearcut as it may also be associated with the Néel transition.

factor 1.25 ± 0.03 and corrected by a difference in residual resistivity of $0.22\,\mu\Omega$cm. The former number allows to estimate the uncertainty in the determination of the sample dimensions, *i.e.*, the systematic standard error for the geometry factor. It is about 2.5%, and it is the same for all measurements. The thermal and electrical transport coefficients were measured on the same sample (sample 1) with the same contact configuration, and the Lorenz ratio $L(T)/L_0 = \rho(T)/w(T)$ is affected by an additional systematic error of about 4.5% due to the finite width of the contacts, see Section II. Thus, a total systematic error of 7% has to be considered, *i.e.*, it will shift systematically all curves of Fig. 3 of the main text. This explains why in the region of the field-induced Fermi-liquid in the phase diagram, *e.g.*, at $B \geq 0.6$ T and below $T = 0.15$ K, the difference $w(T) - \rho(T)$ is not exactly zero, and the Lorenz ratio does not reach exactly one.

IV. ELECTRICAL RESISTIVITY

The electrical resistivity $\rho(T)$ was determined by a four-point ac-technique in a ^{3}He-^{4}He dilution refrigerator down to $T \approx 0.02$ K. Figure S1 shows the resistivity data of samples 1 and 2 at $B = 0$ and 0.1 T, respectively. The data for the second sample, which has a lower residual resistivity, have been scaled as described above. The data agree nicely, and we conclude that both samples show the same overall behaviour. The slightly larger resistivity in the zero-field curve below 0.05 K for sample 1 is due to heating effects. Therefore, the second sample was measured at different currents to investigate the influence of the current on the curvature of $\rho(T)$. The results below 0.1 K are displayed in the inset of Fig. S2 plotted as a function of T^2, a temperature dependence expected below $T_N = 0.07$ K for $B = 0$ (Ref. 6). The heating effect can be neglected at a current of 5 μA. We used the resistivity data with this current to evaluate the Lorenz ratio. As will be shown in a forthcoming paper,[7] the heating effect is particularly strong in the vicinity of B_c. In addition, it is increasing with increasing residual resistivity ρ_0. For a single crystal of very high perfection with $\rho_0 \approx 0.5$ $\mu\Omega$ cm, no heating effect could be observed down to $T \approx 0.02$ K using a current of 50 μA (Ref. 8). In this case, $\Delta\rho \sim T$ was observed below $T = 0.1$ K down to the lowest accessible temperature of 0.02 K.

In all samples the magnetoresistivity was measured and compared to that of the samples investigated in Refs. 9,10, to assure consistency of the properties observed in our samples with those of the best single crystals grown so far. As an example, the magnetoresistivity of sample 2 is shown in Fig. S3: At $T = 0.03$ K the change in resistivity associated with the crossover is about 10% (see insets of the same figure), as also found in the samples studied in Ref. 9 (*cf.* Fig. S5 of the Supporting Information of Ref. 9). The dominant feature is a rapid crossover across B^*, corresponding to a jump in the zero-temperature limit[9,10]. The isothermal resistivity vs. the magnetic field at low temperatures are also consistent with the existence of a peak near B^* as a secondary feature superimposed on the sharp jump, although it could

also be associated with the (classical) Néel transition.

V. THERMAL CONDUCTIVITY

A. Experimental details

The thermal conductivity $w(T)$ was measured using a steady-state two-thermometer, one-heater technique in a ^{3}He-^{4}He dilution refrigerator down to $T \approx 0.025$ K. The heat loss along the wires and suspensions for thermometers and heater is estimated to be a factor of 1000 smaller than the heat flow through the sample. κ was calculated from the electrical power P released by a resistive heater, the temperature difference ΔT between two contacts on the sample and the geometry factor A as $\kappa = A \cdot P/\Delta T$. ΔT was measured by two RuO_2 resistance thermometers, that were calibrated against the primary ("cold finger") sensor during each temperature run, using the resistances measured at zero heating power. A stability of better than 0.1 % of both sample temperature readouts was achieved in the entire measurement range. For each stabilized bath temperature a set of four different heat currents was applied which results in temperature gradients $\Delta T/T = 1\%$ - 7% along the sample. The proportionality between the applied heater power and the achieved temperature gradients at a constant bath temperature proves that the system is in the regime of linear response. The resulting raw data of κ were then averaged. Our measurement procedure implies the following uncertainties: i) The uncertainty in A represents a systematic error, that shifts all $\kappa(T)$ curves by a constant factor, as described in Section III; ii) the uncertainty in P is negligible because current and voltage at the heater can be measured with high accuracy; iii) the uncertainty in ΔT results from the measurement of the thermometer resistances and from errors in the calibration. Concerning the last point, two or more temperature runs have been performed at many fields, each with its own calibration. For a given field, the calculated $\kappa(T)$ values fall on top of each other within the scattering of the data. Therefore, the error in the calibration is negligible compared to the data scattering. In fact, the largest uncertainty arises from the measurement of the thermometer resistances due to the limited excitation current, especially at low T. It leads to scattering of the raw data and is significantly reduced in our final data by averaging over several points. As error bars we took the standard deviation of the raw data as displayed in Figs. 2 and 3 of the main text as well as Figs. S4 and S5. The systematic error due to the sample and contact geometry is not included, because it results only in a shift of all curves as explained in Section III. We attribute the observation of w_0 being about 1% larger than ρ_0 in the Fermi liquid regime at high fields (Figs. 2**d** and S4**f**) to this systematic error.

Finally, the noise level in the data of the thermal resistivity increases substantially with increasing magnetic field, as can be directly seen in Fig. S4. It is presumably due to the vibrations of the set-up wires in magnetic fields. This is the main reason why we could not perform reliable measurements below 0.06 K at fields larger than 0.06 T.

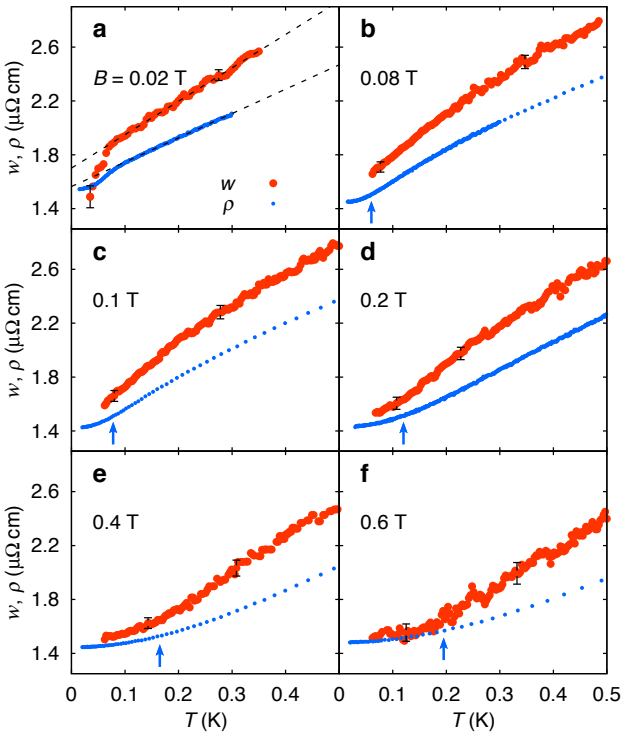

FIG. S4: Thermal and electrical resistivity $w = L_0T/\kappa_{el} \approx L_0T/\kappa$ and ρ plotted as a function of temperature, at $T \leq 0.5$ K for $B = 0.02$ T **a**, 0.08 T **b**, 0.1 T **c**, 0.2 T **d**, 0.4 T **e** and 0.6 T **f** ($B \perp c$). The arrows in **b** through **f** indicate the crossover to Fermi-liquid behaviour (*cf.* Fig. 1**a** of the main text). A significant drop is seen in the residual ($T \to 0$) thermal and electrical resistivities when going from $B = 0.02$ T **a** to 0.08 T **b** and 0.1 T **c**, which parallels the drop in the isothermal magnetoresistivity across B_c (*cf.* Fig. S3) as previously observed and attributed to an abrupt increase in the charge carrier concentration.[9,10] Also, the slight rise of the residual thermal and electrical resistivities upon increasing field (*cf.* **d** through **f**) confirms the trend observed in Ref. 10 and ascribed there to the magnetoresistivity in the paramagnetic phase of $YbRh_2Si_2$.

B. Phonon contribution

The phonon contribution, $\kappa_{ph}(T)$, to the measured thermal conductivity $\kappa(T)$ can be separated from the electronic part, $\kappa_{el}(T)$, by avoiding the low-temperature range where a significant inelastic scattering of the charge carriers has been evidenced (*cf.* Fig. 1**b** of the main text and Ref. 4).

After having subtracted $\kappa_{el}(T) = \kappa_{WF}(T) =$

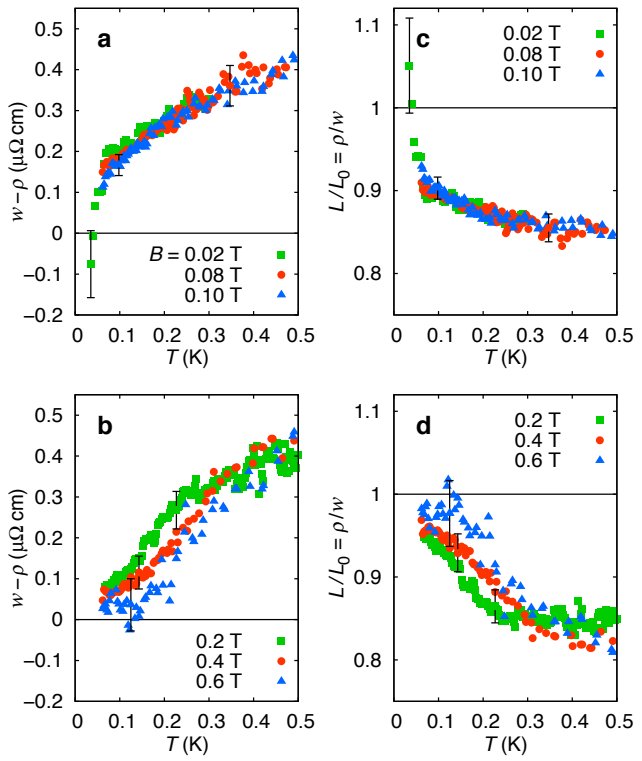

FIG. S5: Difference $(w - \rho)$ vs T at $B = 0.02\,\mathrm{T}$, $0.08\,\mathrm{T}$ and $0.1\,\mathrm{T}$ **a** as well as $0.2\,\mathrm{T}$, $0.4\,\mathrm{T}$ and $0.6\,\mathrm{T}$ **b**. **c**, **d** Lorenz ratio $L/L_0 = \rho/w$ vs T for the same fields as in **a**, **b**. The data for $B = 0.02\,\mathrm{T}$ are similar to those for $B = 0$ (*cf.* Figs. 3**a** and **c** of the main text). They provide convincing evidence for an extra heat channel which adds to the one of the electronic quasiparticles and ist most likely due to AF magnons (see text). For $B = 0.6\,\mathrm{T}$ a Fermi-liquid phase forms below $T \approx 0.15\,\mathrm{K}$. This can also be anticipated for $B = 0.4\,\mathrm{T}$ and $0.2\,\mathrm{T}$ and even for $B = 0.1\,\mathrm{T}$ and $0.08\,\mathrm{T}$ at correspondingly lower crossover temperatures.

$L_0T/\rho(T)$ from $\kappa(T)$ for $6\,\mathrm{K} < T < 12\,\mathrm{K}$, *i.e.*, assuming the validity of the Wiedemann-Franz (WF) law to hold in this temperature range for the electronic heat transport, the phonon contribution $\kappa_{\mathrm{ph}}(T)$ is found to follow a T^{ϵ} dependence with $\epsilon = 2 \pm 0.2$. As shown in Fig. 1**b**, main text, an extrapolation of this power law to lower temperatures indicates a negligible $\kappa_{\mathrm{ph}}(T)$ below $1\,\mathrm{K}$, *i.e.*, within the temperature range of interest in the present work. The uncertainty in the exponent has only little effect on the estimated $\kappa_{\mathrm{ph}}(T)$ below $5\,\mathrm{K}$. The insignificance of $\kappa_{\mathrm{ph}}(T)$ below $1\,\mathrm{K}$ is further corroborated by the almost constant Lorenz ratio $L/L_0 \approx 0.86$ within the range $0.5\,\mathrm{K} < T < 1\,\mathrm{K}$, presumably associated with a measured thermal conductivity of purely electronic origin. Assuming this Lorenz ratio to extend to above $2\,\mathrm{K}$, $\kappa_{\mathrm{el}}(T) = LT/\rho(T)$ can easily be estimated. Subtracting this from the measured $\kappa(T)$, the phonon part is obtained once more. Below about $5\,\mathrm{K}$, $\kappa_{\mathrm{ph}}(T)$ obtained by the latter procedure is found to be in very good agreement with that from the former one.

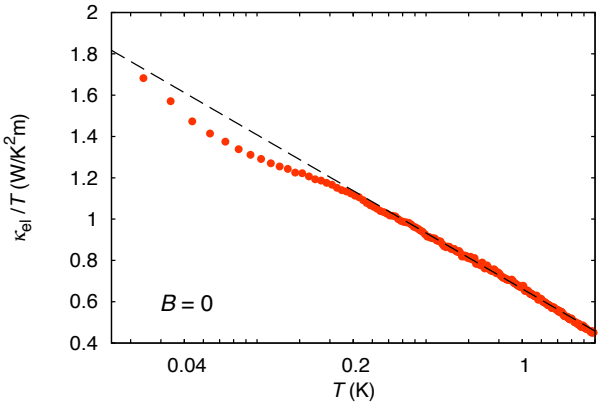

FIG. S6: Temperature coefficient of the $B = 0$ electronic thermal conductivity, κ_{el}/T, of $YbRh_2Si_2$ plotted as a function of T on a logarithmic scale to emphasize that it follows a logarithmic behaviour on cooling from $2\,\mathrm{K}$ to about $0.3\,\mathrm{K}$.

We, therefore, conclude that below about $10\,\mathrm{K}$, $\kappa_{\mathrm{ph}}(T)$ of $YbRh_2Si_2$ follows a T^2 dependence, as commonly expected for a metal in this temperature range due to dominating phonon scattering from the conduction electrons.[11] A nearly T^2-dependence of $\kappa_{\mathrm{ph}}(T)$ has indeed been observed for several heavy-fermion compounds, e.g., CeB_6,[12] $CeNiSn$[13] and $CeAuAl_3$[14] in a similar temperature range. In these systems the dominant phonon wavelength, λ_{ph}, is assumed to be shorter than the mean free path of charge carriers, l_{el}, Ref. 15. This assumption, thus, appears to hold also for the $YbRh_2Si_2$ single crystal studied here. On the other hand, for $CeCu_2Si_2$,[16] $CeAl_3$[17] and $CeCu_6$[18] $\kappa_{\mathrm{ph}}(T)$ depends almost linearly on T, which hints at the opposite relation between λ_{ph} and l_{el}, *i.e.*, $\lambda_{\mathrm{ph}} > l_{\mathrm{el}}$, Ref. 15.

C. Electronic contribution

The thermal conductivity obtained by subtracting $\kappa_{\mathrm{ph}}(T)$ from the measured $\kappa(T)$ is $\kappa_{\mathrm{el}}(T)$. In Fig. S6 we show that the temperature coefficient, κ_{el}/T, increases logarithmically upon cooling from $T = 2\,\mathrm{K}$ to about $0.3\,\mathrm{K}$. A corresponding logarithmic divergence was observed also for the Sommerfeld coefficient of the electronic specific heat, $\gamma = C_{\mathrm{el}}/T$,[19,20] and the thermopower coefficient S/T.[21]

In the following, we are interested in the corresponding thermal resistivity $w(T) = L_0T/\kappa_{\mathrm{el}}(T)$, which is displayed together with $\rho(T)$, in Fig. 2 of the main text for four different fields. The results of $w(T)$ and $\rho(T)$ for other magnetic fields are shown in Fig. S4. The data taken at $B = 0.08\,\mathrm{T}$ through $0.6\,\mathrm{T}$ are complementary to those at $B = 0.3\,\mathrm{T}$ and $1\,\mathrm{T}$ presented in Figs. 2**c** and 2**d** of the main text. The data at $B = 0.02\,\mathrm{T}$ are likewise complementary to those at zero field presented in Fig. 2**a** of the main text. Like in the zero-field case, they show a low-temperature downturn in the AF phase

which contains the magnon contribution to the heat conduction. Figure S5 displays the difference $w(T) - \rho(T)$ **a**,**b** and the ratio $\rho(T)/w(T) = L/L_0$ **c**,**d** for the data shown in Fig. S4. The existence of a magnon contribution to the thermal conductivity at $B = 0.02\,\mathrm{T}$ is indicated by $(w - \rho)$ being negative and L/L_0 being larger than one below $T \approx 0.03\,\mathrm{K}$, very similar to the results at $B = 0$ (*cf.* Figs. 3**a** and 3**c** of the main text). Within the experimental uncertainties, the data at $B = 0.6\,\mathrm{T}$ indicate Fermi-liquid behaviour and the validity of the WF law below $T \approx 0.15\,\mathrm{K}$. Fermi-liquid behaviour below a crossover temperature which continuously decreases with decreasing magnetic field is inferred for both $B = 0.4\,\mathrm{T}$ and $0.2\,\mathrm{T}$ **b**,**d**. This implies $L/\mathrm{L}_0 \to 1$ as $T \to 0$, with which also the results obtained for $B = 0.1\,\mathrm{T}$ and even $0.08\,\mathrm{T}$ are compatible **a**,**c**.

The data for w and ρ measured as a function of temperature for fixed magnetic fields, shown in Fig. 2 of the main text and Fig. S4, have been used to determine the isothermal Lorenz ratio as a function of field displayed in Fig. 3**e** of the main text. The isothermal field dependence exhibits a minimum near B^*. This striking behaviour is also seen in preliminary results obtained from direct isothermal measurements of w and ρ as a function of field in a sample with lower residual resistivity[22].

D. Magnon contribution

For the measurements performed at $B = 0$ (Fig. 2**a**, main text) as well as $0.02\,\mathrm{T}$ (Fig. S4**a**) a downturn in the thermal resistivity is found below $T \approx 0.1\,\mathrm{K}$ and $T \approx 0.08\,\mathrm{K}$, respectively, while at $B = 0.06\,\mathrm{T}$ a similar but smaller feature occurs below $T \approx 0.07\,\mathrm{K}$ (Fig. 2**b**, main text). One may ascribe this drop in $w(T)$ to the freezing out of inelastic scatterings provided by spin fluctuations in the electronic heat transport. However, while ferromagnetic spin fluctuations remain unchanged, antiferromagnetic ones grow at sufficiently low temperatures and magnetic fields, as inferred from NMR Knight shift and spin-lattice relaxation rate measurements, respectively.[23] Therefore, the only natural interpretation of this drop involves heat carriers which add to the electronic ones. The existence of a corresponding excess contribution to the thermal conductivity, $\Delta\kappa(T)$, is proven by our observation that for $B = 0$ and $B = 0.02$ T the thermal resistivity becomes smaller than the electrical resistivity, *cf.* Figs. 2**a** and S4**a**. $\Delta\kappa(T)$ adds to $\kappa_{\mathrm{el}}(T)$ which we assume to be given by $L_0 T/\rho$ at temperatures well below T_{N}, *i.e.*, we assume the Wiedemann-Franz law to describe the electronic transport in the Fermi-liquid phase well below T_{N}. The observed $\Delta\kappa(T)$ falls into the range $2-5\cdot10^{-3}\,\mathrm{W/Km}$ between 0.025 and 0.03 K. Because this value of $\Delta\kappa$ is close to the experimental uncertainty, its temperature dependence is hard to be experimentally determined. Nevertheless, its existence has been confirmed by repeated measurements. Lattice vibrations are unapt to account for this extra thermal conductivity, as the largest expected κ_{ph}, which is limited by the sample dimension ($\approx 100\,\mu\mathrm{m}$) and, employing the lattice specific heat,[20] is estimated to be less than $1\cdot10^{-5}\,\mathrm{W/Km}$ in this range.

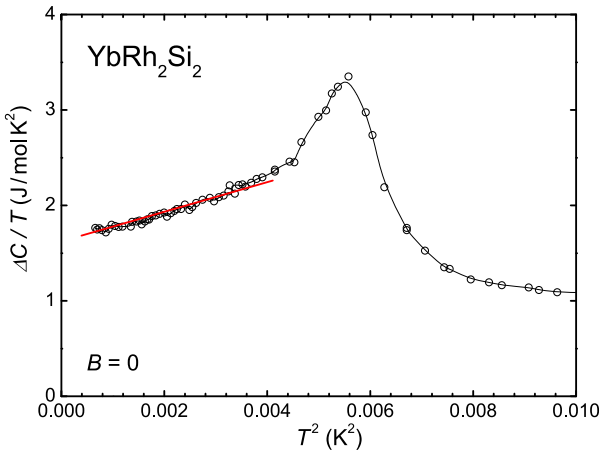

FIG. S7: Specific heat of $YbRh_2Si_2$, shown as $\Delta C/T$ versus T^2. $\Delta C(T) = C(T) - C_{\mathrm{ph}}(T) - C_{\mathrm{Q}}(T)$, where $C_{\mathrm{ph}}/C_{\mathrm{Q}}$ denotes the phonon/nuclear quadrupole contribution. The red line indicates a T^3 contribution to ΔC below 0.05 K.[20]

Another potential thermal heat channel is that of AF magnons. The signature of these spin-wave excitations was clearly observed [20] in the zero-field specific heat examined down to $T = 0.018\,\mathrm{K}$ for an $YbRh_2Si_2$ single crystal being of similar quality as samples 1 and 2. As seen in Fig. S7, below $T = 0.05\,\mathrm{K}$ the specific heat can be described by $\Delta C = C - C_{\mathrm{ph}} - C_{\mathrm{Q}} = \gamma T + \beta T^3$, with C_{ph} and C_{Q} being, respectively, the phonon and the nuclear quadrupole contributions, $\gamma = 1.64\,\mathrm{J/(K^2 mol)}$ and $\beta = 132.2\,\mathrm{J/(K^4 mol)}$. The huge electronic contribution $C_{\mathrm{el}} = \gamma T$ denotes a heavy Landau FL phase.[20] The Debye-like term $C_m \sim T^3$ is characteristic of the contribution of long-wavelength AF acoustic magnons. In the framework of the Debye theory and using the measured β value, we can estimate the "magnetic Debye temperature", Θ_m, and the group velocity v_m of the magnons to be 4.2 K and 36 m/s, respectively. This Debye temperature corresponds to the AF exchange interaction suitably averaged over the three main spatial directions. The extracted group velocity is substantially smaller than that for typical Ce-based heavy-fermion AF metals, *e.g.*, about one-tenth of the corresponding value for $CeAl_2$,[24] reflecting both the averaging over the spatial directions as well as the weak Néel order of $YbRh_2Si_2$. The classical kinetic relation, $\kappa_m = (1/3) C_m v_m l_m$ (l_m: magnon mean free path), allows to estimate the magnon contribution to the thermal conductivity, κ_m. In order to obtain a κ_m of $2 - 5\cdot10^{-3}\,\mathrm{W/Km}$ in the range $0.025 - 0.03\,\mathrm{K}$ as observed in Fig. 2**a** of the main text and Fig. S4**a**, the corresponding magnon mean free path l_m has to be in the range of $2-13\,\mu\mathrm{m}$. Since in the low-temperature limit l_m is expected to be equal in size to that of the AF domains,

the latter are estimated to be of the order of a few μm below about 0.03 K which, indeed, is a reasonable order of magnitude.[25]

The less pronounced downturn in $w(T)$ observed below $T = 0.07$ K at $B = 0.06$ T (Fig. 2**b**, main text) is ascribed to overdamped AF magnons, which were shown, via inelastic neutron scattering experiments,[26,27] to exist for antiferromagnetically ordered materials substantially above the Néel temperature. Heat transport by short-lived magnon excitations has been reported, e.g., for the parent compound of the 214 high-T_c cuprates, La_2CuO_4, an $S = 1/2$, 2D antiferromagnet with a Néel temperature $T_N \approx 310$ K.[28] In particular, $S = 1$ chain systems, like Y_2BaNiO_5 (Ref. 29) and $Ni(C_2H_8N_2)_2NO_2(ClO_4)$ (NENP) (Ref. 30) have served as model systems in this context.

We would like to note that the magnon contribution cannot be avoided by performing thermal Hall measurements. In contrast to the case of phonons,[2] magnons may generate a transverse thermal gradient.[31]

VI. EXTRAPOLATION OF THE LORENZ RATIO TO ZERO TEMPERATURE IN QUANTUM CRITICAL SYSTEMS

We now discuss the various isofield and isothermal scans that are used for the extrapolation of the Lorenz ratio in the vicinity o a QCP. We will discuss the special case that is pertinent to $YbRh_2Si_2$, namely a field-induced QCP separating an AF ordered phase and a paramagnetic Fermi-liquid phase.

Fig. S8**a** illustrates different temperature scans in different parts of the phase diagram. Scan A starts from the quantum critical regime, but runs into the ordered phase; by construction, it passes through the phase boundary. The zero-temperature limit of $w(T)$, $\rho(T)$ and $L(T)/L_0$ so extrapolated does not reflect the quantum critical behavior, but instead only captures that of the ordered phase. Scan B also starts from the quantum critical regime, but runs into the low-temperature paramagnetic Fermi liquid phase; it passes through a crossover temperature. Again, the zero-temperature limit so extrapolated does not reflect the quantum critical behavior, but instead only captures that of the paramagnetic Fermi liquid phase. Scan C starts from the quantum critical regime, and goes all the way to the QCP as the temperature is lowered. The zero-temperature limit so extrapolated captures the properties of the QCP. In practice, however, the same purpose can be achieved by carrying out scans C_1 or C_2 (provided there is enough dynamical range in temperature). These start in the quantum critical regime but stop before running into the Néel temperature or the crossover temperature to the paramagnetic Fermi liquid region. The zero-temperature limit so extrapolated also manifests the behavior of the QCP.

The different temperature scans will also be manifested in the isothermal properties of L/L_0 as a function of the control parameter, as illustrated in Fig. S8**b**. Scan a starts from the paramagnetic Fermi-liquid regime, and runs into the quantum critical regime. As it passes through the crossover scale between the two regimes, we expect to see a crossover in L/L_0 in a way that compliments what is seen in the temperature scan B. Scan B starts from the paramagnetic Fermi-liquid regime, passing through the quantum critical regime, and runs into the ordered phase. Because it passes through both the crossover temperature and the Néel temperature lines, this isothermal scan will reflect the features of both temperature scan B and temperature scan A.

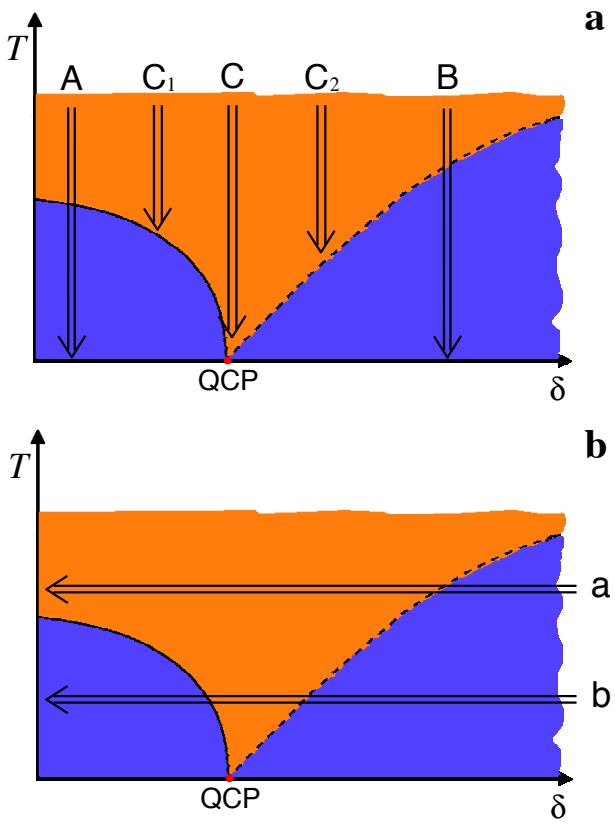

FIG. S8: Isofield **a** and isothermal **b** scans for the extrapolation of the Lorenz ratio in the vicinity of a QCP, as described in detail in the text.

In this work, our primary focus is on temperature scans C_1 (Figs. 2**a**, 3**a**, 3**c**), scans close to C (Fig. 2**b**), and scans C_2 (*e.g.* Figs. S4**b** and **c**) through B (Figs. 2**c**, 2**d**, 3**b**, 3**d**). In addition, isothermal scans a (Fig. 3**e**) are conducted. Because of the masking effect of magnons on the electronic heat transport, we do not attempt to analyze any scan b. Temperature scans A cannot be performed in $YbRh_2Si_2$ because of the small value of the critical field B_c.

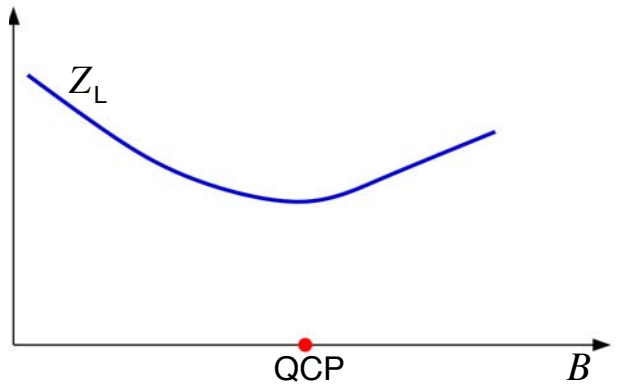

FIG. S9: The evolution of the quasiparticle weights across a heavy-fermion spin-density-wave quantum critical points. Z_L of the large Fermi surface stays nonzero as the system is tuned through the QCP.

VII. THEORETICAL ASPECTS

The validity of the WF law in the vicinity of a heavy-fermion spin-density-wave QCP was briefly discussed in the main text. Across such a QCP, the heavy quasiparticles remain intact in the main part of the Fermi surface. In these "cold" regions, the quasiparticles do not experience scattering by the AF spin fluctuations, and their spectral weight—the quasiparticle residue Z—stays finite as the control parameter moves through the QCP (Fig. S9). L/L_0 must be equal to one in this case. Even the contributions from the "hot" regions, which experience scatterings by the bosonic collective fluctuations, cannot violate the WF law, as was illustrated by the case of $ZrZn_2$ (Ref. 1) where ferromagnetic fluctuations influence the entire Fermi surface.

This is in contrast to the Kondo-destroying local quantum critical description which is illustrated in Fig. 4 of the main text. In the paramagnetic Fermi-liquid state, the conduction electron self-energy, $\Sigma(\boldsymbol{k}, \omega, T)$ contains a pole at the Kondo-resonance energy. It converts the f-moments into a part of the Landau quasiparticles, thereby creating a large Fermi surface. The quasiparticle residue at the large Fermi momenta, $\boldsymbol{k}_{\rm F}^{\rm L}$, is nonzero, $Z_L(\boldsymbol{k}_{\rm F}^{\rm L}, \omega = 0, T = 0) \neq 0$. In the AF Fermi-liquid state, the Kondo resonance is destroyed. The Fermi surface is given by that of the conduction electrons only in the presence of a staggered magnetic field. Away from the "hot spots", there are Landau quasiparticles associated with a small Fermi surface. The quasiparticle residue at such generic small Fermi momenta, $\boldsymbol{k}_{\rm F}^{\rm S}$, is nonzero, $Z_S(\boldsymbol{k}_{\rm F}^{\rm S}, \omega = 0, T = 0) \neq 0$.

In these Fermi-liquid regimes, both the electrical and electronic heat currents are predominantly carried by Landau quasiparticles. At nonzero temperatures, the electronic heat carriers experience inelastic scatterings. Because the non-Umklapp processes are considerably more efficient in relaxing electronic heat current than electrical current, even in anisotropic systems at low temperatures, the electron-electron scatterings lead to an electronic Lorenz ratio $L_{\rm el}/L_0 < 1$ at nonzero temperatures.[32] The effect is similar to the usual case of electron-phonon scattering.[11] The Umklapp scatterings are expected to contribute equally efficiently to the thermal and electrical resistivities. In the zero-temperature limit, well-defined quasiparticles remain, but the inelastic scatterers are frozen out; only the elastic scattering processes remain, and $L_{\rm el}/L_0$ is equal to 1. This is illustrated in Fig. S10, where $L_{\rm el}/L_0$ reaches 1 as the system moves away from the QCP (at B_c) into the Fermi-liquid regimes on both sides.

In the quantum critical regime, low-energy electronic excitations occur at both the small and large Fermi surfaces (Fig. 4, main text). The single-electron self-energy at both $\boldsymbol{k}_{\rm F}^{\rm S}$ and $\boldsymbol{k}_{\rm F}^{\rm L}$ vanishes at the $\omega = 0$ and $T = 0$ limit, but has the scaling form as a function of ω and T as given in Eq. 1 (main text). This reflects the fluctuations of the Fermi surfaces, which characterize the quantum fluctuations in the *entire* quantum critical regime. We will consider the electrical and heat currents carried by the electronic excitations at both $\boldsymbol{k}_{\rm F}^{\rm S}$ and $\boldsymbol{k}_{\rm F}^{\rm L}$, all of which are non-Fermi liquid in nature as specified by Eq. 1. These electronic current carriers are subject to inelastic scatterings that are associated with the quantum criticality. While such scattering processes are many-body in nature, they can still be divided into Umklapp and non-Umklapp processes. The non-Umklapp processes will contribute considerably more to the thermal resistivity than to the electrical resistivity. As a result, $L_{\rm el}/L_0$ will be less than 1.

The end result is a dip of $L_{\rm el}/L_0$ near B_c. Fig. S10 illustrates the corresponding isothermal behaviour of $L_{\rm el}/L_0$ for a given nonzero but low T, where the dip is expected to be centered at $B^*(T) = B(T^*)$, *cf.* Fig 1**a** of the main text. As $T \to 0$, the dip becomes abrupt at B_c.

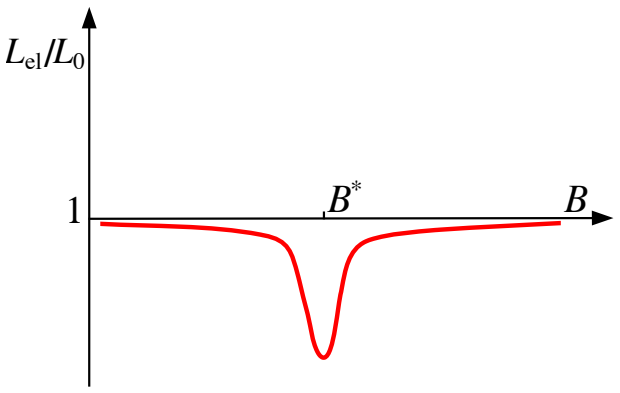

FIG. S10: Expected isothermal behaviour of the Lorenz ratio across a Kondo-destroying QCP. $B^*(T) = B(T^*)$ is the Kondo breakdown scale at a nonzero but small T. At zero temperature an abrupt dip occurs at $B^* = B_c$

[1] Smith, R. P. *et al.* Marginal breakdown of the Fermi-liquid state on the border of metallic ferromagnetism. *Nature* **455**, 1220-1223 (2008).

[2] Wakeham, N. *et al.* Gross violation of the Wiedemann-Franz law in a quasi-one-dimensional conductor. *Nature Commun.* **2**, 396–401 (2011).

[3] Tanatar, M. A., Paglione, J., Petrovic, C. & Taillefer, L. Anisotropic violation of the Wiedemann-Franz law at a quantum critical point. *Science* **316**, 1320-1322 (2007).

[4] Tomokuni, K. *et al.* Thermal transport properties and quantum criticality of heavy fermion $YbRh_2Si_2$. *J. Phys. Soc. Jpn.* **80**, Supplement A SA096 (2011).

[5] Seyfarth, G. *et al.* Multiband superconductivity in the heavy fermion compound $PrOs_4Sb_{12}$. *Phys. Rev. Lett.* **95**, 107004 (2005).

[6] Gegenwart, P. *et al.* Magnetic-field induced quantum critical point in $YbRh_2Si_2$. *Phys. Rev. Lett.* **89**, 056402 (2002).

[7] Lausberg, S. *et al.*, to be published (2012).

[8] Westerkamp, T. Quantenphasenübergänge in den Schwere-Fermionen-Systemen $Yb(Rh_{1-x}M_x)_2Si_2$ und $CePd_{1-x}Rh_x$. PhD Thesis (TU Dresden, 2008).

[9] Friedemann, S. *et al.* Fermi-surface collapse and dynamical scaling near a quantum critical point. *Proc. Natl. Acad. Sci. USA* **107**, 14547-14551 (2010).

[10] Friedemann, S. *et al.* Discontinuous Hall coefficient at the quantum critical point in $YbRh_2Si_2$. *J. Phys.: Condens. Matter* **23**, 094216 (2011).

[11] Ziman, J. M. Electron and phonons *Clarendon Press* (1960).

[12] Peysson, Y. *et al.* Thermal properties of CeB_6 and LaB_6. *J. Magn. Magn. Mat.* **47–48**, 63–65 (1985)

[13] Kitagawa, J. *et al.* Effects of valence fluctuation and pseudogap formation on phonon thermal conductivity of Ce-based compounds with ϵ-TiNiSi-type structure. *Phys. Rev. B* **66**, 224304 (2002).

[14] Aoki, Y. *et al.* Thermal conductivity of $CeAuAl_3$: Evidence of phonon scattering by Ce magnetic moment fluctuations. *Phys. Rev. B* **62**, 87–90 (2000).

[15] Zimmerman, J. E. Low-temperature lattice heat conduction in high-resistivity alloys. *J. Phys. Chem. Sol.* **11**, 299–302 (1959).

[16] Franz, W., Grießel, A., Steglich, F. & Wohlleben, D. Transport properties of $LaCu_2Si_2$ and $CeCu_2Si_2$ between 1.5 K and 300 K. *Z. Phys. B* **31**, 7-17 (1978).

[17] Ott, H. R., Marti, O. & Hulliger, F. Low temperature thermal conductivity of $CeAl_3$. *Solid State Commun.* **49**, 1129–1131 (1984).

[18] Peysson, Y., Salce, B., Ayache, C. & Bauer, E. Thermal conductivity of $CeCu_6$ and $LaCu_6$. *J. Magn. Magn. Mat.* **54–57**, 423–424 (1986)

[19] Trovarelli, O. *et al.* $YbRh_2Si_2$: Pronounced non-Fermi-liquid effects above a low-lying magnetic phase transition. *Phys. Rev. Lett.* **85**, 626–629 (2000).

[20] Custers, J. *et al.* The break-up of heavy electrons at a quantum critical point. *Nature* **424**, 524–527 (2003).

[21] Hartmann, S. *et al.* Thermopower evidence for an abrupt Fermi surface change at the quantum critical point of $YbRh_2Si_2$. *Phys. Rev. Lett.* **104**, 096401 (2010).

[22] Pfau, H. *et al.*, to be published (2012).

[23] Ishida, K. *et al.* $YbRh_2Si_2$: Spin fluctuations in the vicinity of a quantum critical point at low magnetic field. *Phys. Rev. Lett.* **89**, 107202 (2002).

[24] Bredl, C. D., Steglich, F. & Schotte, K. D. Specific heat of concentrated Kondo systems: $(La,Ce)Al_2$ and $CeAl_2$. *Z. Phys. B* **29**, 327–340 (1978).

[25] For example, the AF domain size is roughly 16 μm for elemental chromium (Werner, S. A. *et al.*, *Phys. Rev.* **155**, 528–539 (1967)), and is $\approx 1\mu$m for the $5f$-based heavy-fermion compound UPt_3 (de Visser, A. *et al.*, *J. Magn. Magn. Mat.* **177**, 287–291 (1998)).

[26] Wiltshire, M. C. K. & Elcombe, M. M. Temperature dependence of magnons in γ-MnCu. *J. Magn. Magn. Mat.* **31–34**, 127–128 (1983).

[27] Wiltshire, M. C. K., Elcombe, M. M. & Howard, C. J. Temperature dependence of the magnetic excitations in γ-$Mn_{90}Cu_{10}$. *J. Phys. F: Met. Phys.* **15**, 1595–1611 (1983).

[28] Hess, C. *et al.* Magnon heat transport in doped La_2CuO_4. *Phys. Rev. Lett.* **90**, 197002 (2003).

[29] Kordonis, K. *et al.* Spin thermal conductivity of the Haldane chain compound Y_2BaNiO_5. *Phys. Rev. Lett.* **97**, 115901 (2005).

[30] Sologubenko, A. V. *et al.* Field-dependent thermal transport in the Haldane chain compound NENP. *Phys. Rev. Lett.* **100**, 137202 (2008).

[31] Onose, Y. *et al.* Observation of the magnon Hall effect. *Science* **329**, 297 (2010).

[32] Herring, C. *et al.* Simple property of electron-electron collisions in transition metals. *Phys. Rev. Lett.* **19**, 167 (1967).